



Carbon nanofiber/cobalt oxide nanopyramid core–shell nanowires for high-performance lithium-ion batteries



Geon-Hyoung An, Hyo-Jin Ahn*

Department of Materials Science and Engineering, Seoul National University of Science and Technology, Seoul 139-743, Republic of Korea

HIGHLIGHTS

- Carbon nanofiber (CNF)/cobalt oxide nanopyramid core–shell nanowires (NWs).
- Introduction of CoO seed-loaded CNFs for uniform and dense Co₃O₄ nanopyramids.
- Synergistic effect of 1-D CNFs, Co₃O₄ nanopyramids, and the geometric networks.

ARTICLE INFO

Article history:

Received 11 July 2014

Received in revised form

2 September 2014

Accepted 7 September 2014

Available online 16 September 2014

Keywords:

Li-ion battery

Carbon nanofiber

Cobalt oxide nanopyramid

Core–shell nanowires

Anode

ABSTRACT

Carbon nanofiber (CNF)/Co₃O₄ nanopyramid core–shell nanowires (NWs) are synthesized using an electrospinning method followed by reduction and hydrothermal treatment in order to improve the capacity, cycle stability, and high-rate capability of the electrodes in Li ion batteries (LIBs). The morphology, crystal structure, and chemical states of all samples are investigated by means of field emission scanning electron microscopy, transmission electron microscopy, X-ray diffraction, X-ray photoelectron spectroscopy, and thermogravimetric analysis. For comparison, conventional CNFs, octahedral Co₃O₄, and Co₃O₄/CNF composite electrodes are prepared. LIB cells fabricated with the CNF/Co₃O₄ nanopyramid core–shell NWs exhibit superb discharge capacity (1173 mAh g⁻¹ at the 1st cycle), cycle stability (795 mAh g⁻¹ at 50 cycles), high initial Coulombic efficiency (84.8%), and high-rate capability (570 mAh g⁻¹ at a current density of 700 mA g⁻¹) as compared to the conventional CNF, octahedral Co₃O₄, and Co₃O₄/CNF composite electrodes. The performance improvement is owing to the introduction of one-dimensional CNFs relative to efficient electron transport in the core region, extensive utilization of Co₃O₄ nanopyramids with high capacity grown closely on the CNFs in the shell region, and the network structures of the electrode relative to the improvement of Li ion diffusion.

© 2014 Elsevier B.V. All rights reserved.

1. Introduction

Li-ion batteries (LIBs), which are widely applied for portable electronics and potential energy systems such as mobile phones, tablet PCs, robotics, and electric vehicles, have generated considerable interest because of advantages such as their high energy density, good cycling performance, lack of memory effects, and low toxicity [1–6]. In general, LIBs are composed of an anode, a cathode, an electrolyte, and a separator. Among these components in LIBs, development of an anode material will be one of the important core technologies to improve the electrochemical performance of LIBs. Until now, various anode materials such as carbon-based materials [i.e., graphite, graphene, carbon nanotubes (CNTs), and carbon

nanofibers (CNFs)], metal-based or Si-based materials (i.e., LiAl, LiSn, SnCo, SnNi, LiSi, and SiTi), and oxide materials (i.e., Co₃O₄, Fe₂O₃, SiO, and NiO) have been actively studied [7]. In particular, anodes that include transition metal oxides (i.e., Co₃O₄, SnO₂, TiO₂, Fe₂O₃, CuO, and MnO₂) have received considerable attention because they facilitate the fabrication of high-performance LIBs [8–13]. Most of all, cobalt oxide (Co₃O₄) is an excellent candidate for LIB electrodes because of its high theoretical capacity (890 mAh g⁻¹) [14]. However, in spite of its high capacity, researchers have demonstrated that Co₃O₄ electrodes possess poor cycle stability and poor high rate performance because of their large volume change, significant aggregation, and low electrical conductivity during the charge/discharge process [15]. To solve these problems, many different strategies have been tried [16–25]. One of these was to develop a composite electrode consisting of Co₃O₄ and carbon-based materials, i.e., Co₃O₄/graphite, Co₃O₄/graphene, and Co₃O₄/CNT composites. These materials could not

* Corresponding author. Tel.: +82 2 970 6622; fax: +82 2 973 6657.

E-mail address: hjahn@seoultech.ac.kr (H.-J. Ahn).

only effectively prevent the volume change and aggregation found with Co_3O_4 electrodes but also enhance the electrical conductivity of the electrode [25–29]. For example, Wang et al. synthesized Co_3O_4 electrodes supported on graphite by a solvothermal method, and they reported a reversible discharge capacity of 632 mAh g^{-1} obtained after 100 cycles at a current density of 200 mA g^{-1} and high rate performance [28]. Zhou et al. synthesized octahedral Co_3O_4 threaded by CNTs by using a hydrothermal method. Zhou et al. synthesized octahedral Co_3O_4 threaded by CNTs by using a hydrothermal method. They synthesized the sparse octahedral Co_3O_4 with the empty surface on CNTs; this indicates the utilization deficiency of CNTs having a large surface area. Thus, they displayed a reversible discharge capacity of 720 mAh g^{-1} after 100 cycles, as well as a Coulombic efficiency of 76.3% at a current density of 100 mA g^{-1} [29]. Hence, development of advanced combination structures consisting of transition metal oxides relative to high capacity and carbon-based materials relative to high electrical conductivity will be a key technology for fabricating high-performance LIBs. However, the synthesis of CNF/ Co_3O_4 nanopyramid core–shell NWs using CoO seed-loaded CNFs, which could be useful in high-performance LIBs, has not yet been studied. Therefore, we synthesized a novel anode structure of CNF/ Co_3O_4 nanopyramid core–shell nanowires (NWs) using electrospinning, followed by reduction and hydrothermal treatment, and the relationship between the structural properties of the samples and their electrochemical performance is elucidated. CNFs were used in the core region because of their low cost, large surface area-to-volume ratio ($462 \text{ m}^2 \text{ g}^{-1}$), excellent electrical conductivity (10^2 S cm^{-1}), and superior physical and chemical stability, as well as to their one-dimensional (1-D) nanostructures [30–36].

2. Experimental

2.1. Chemicals

Polyacrylonitrile (PAN, $M_w = 150,000$), *N,N*-Dimethylformamide (DMF), cobalt nitrate ($\text{Co}(\text{NO}_3)_2 \cdot 6\text{H}_2\text{O}$), and hexadecyltrimethylammonium bromide (CTAB) were purchased from Sigma–Aldrich. All chemicals were used without further purification.

2.2. Synthesis of CNF/ Co_3O_4 nanopyramid core–shell NWs

CNF/ Co_3O_4 nanopyramid core–shell NWs were synthesized using electrospinning, reduction, and hydrothermal methods in sequence. First, CNFs as the core support of the NWs were prepared using an electrospinning method. In order to synthesize CNFs, 10 wt % PAN was dissolved in DMF with vigorous stirring for 5 h. Aluminum foil, used as the collector, was vertically placed 15 cm from the 23-gage needle. The working voltage of the power supply was fixed at $\sim 13 \text{ kV}$ with a feed rate of 0.03 mL h^{-1} to collect the PAN nanofibres (NFs). The prepared PAN NFs were stabilized at $280 \text{ }^\circ\text{C}$ for 2 h in air and carbonized at $800 \text{ }^\circ\text{C}$ for 2 h in nitrogen atmosphere. Secondly, CNFs, used to form functional groups such as $-\text{COOH}$, $-\text{OH}$, and $>\text{C}=\text{O}$, were prepared using an acid treatment comprising a mixed solution of HF and HNO_3 [1:1 (v/v)] for 5 h. As a result, the functional groups on the CNFs are possible to the loading of metal and/or oxide nanoparticles supported on CNFs [37–39]. The functionalized CNFs were washed several times with deionized (DI) water and then dried in an oven at $80 \text{ }^\circ\text{C}$ in air. To carry out the reduction, the functionalized CNFs were dispersed in DI water with cobalt nitrate for 1 h. A concentrated NaBH_4 solution (100 mg mL^{-1}) was used as a reducing agent to make CoO seed-loaded CNFs (referred to hereafter as CoO seeds/CNFs). Finally, in order to synthesize CNF/ Co_3O_4 nanopyramid core–shell NWs, CoO seeds/CNFs, cobalt nitrate, and CTAB were dispersed in a mixed

solution of methanol and DI water with vigorous stirring for 2 h. CTAB as a cationic surfactant help the formation of Co_3O_4 nanopyramids from Co^{2+} during a hydrothermal reaction. The solution was then transferred into 80 mL Teflon-lined stainless steel autoclaves. A hydrothermal reaction was performed at $180 \text{ }^\circ\text{C}$ for 24 h. The samples were washed several times with DI water and dried at $80 \text{ }^\circ\text{C}$. The resultant CNF/ Co_3O_4 nanopyramid core–shell NWs ($\sim 0.2 \text{ g}$) were then heated at $250 \text{ }^\circ\text{C}$ for 5 h in air and calcined at $400 \text{ }^\circ\text{C}$ for 2 h in argon atmosphere in order to improve the crystallinity of the Co_3O_4 nanopyramids. For comparison, only octahedral Co_3O_4 were prepared using the above-mentioned hydrothermal method. CoO seeds/CNFs were prepared using electrospinning followed by reduction. Co_3O_4 /CNF composites were also prepared using electrospinning followed by a hydrothermal treatment except a reduction method. We thus synthesized five different types of the samples: octahedral Co_3O_4 , conventional CNFs, CoO seeds/CNFs, Co_3O_4 /CNF composites, and CNF/ Co_3O_4 nanopyramid core–shell NWs.

2.3. Characterization

The structural and morphological properties of the samples were investigated using field emission scanning electron microscopy (FESEM; Hitachi S-4800) and transmission electron microscopy (MULTI/TEM; Tecnai G^2 , KBSI Gwangju Center). The crystallinities and crystal structures of the samples were characterized by X-ray diffractometry (XRD, Rigaku D/Max 2500 V) with Cu $K\alpha$ radiation in the range from 10° to 90° with a step size of 0.02° . The chemical bonding states of the samples were measured using X-ray photoelectron spectroscopy (XPS) analyses by a photoelectron spectrometer (ESCALAB 250) with an Al $K\alpha$ X-ray source under a base pressure of 267 nPa. The contents of the samples were examined by thermogravimetric analysis (TGA-50, Shimadzu) from 100 to $800 \text{ }^\circ\text{C}$ at a heating rate of $10 \text{ }^\circ\text{C min}^{-1}$ in air atmosphere.

2.4. Electrochemical characterization

The electrochemical performance of the samples was evaluated using Li coin cells (CR2032, Hohsen Corporation) composed of the prepared samples as the anode, Li metal foil (Honjo Chemical, 99.8%) as the cathode, a porous polypropylene membrane (Celgard 2400) as the separator, and a 1.0 M LiPF_6 solution in a mixture of ethylene carbonate–dimethyl carbonate (1:1) as an electrolyte. For the anode, slurries consisting of the active materials (80 wt%), Ketjen black (10 wt%) as a conducting material (Alfa Aesar), and poly(vinylidene difluoride) (10 wt%) as a binder (Alfa Aesar) in an *N*-methyl-2-pyrrolidinone solvent (NMP, Aldrich) were coated on a Cu foil substrate (Nippon Foil, $18 \mu\text{m}$). The resultant electrodes were dried in a convection oven at $100 \text{ }^\circ\text{C}$ for 12 h. The Li coin cells were assembled in a high-purity argon-filled glove box ($<5 \text{ ppm}$, H_2O and O_2). The cyclic voltammetry (CV) measurements were carried out using a potentiostat/galvanostat (Autolab PGSTAT302N, FRA32M) in the potential range of 0.0–3.0 V (versus Li/Li^+) at a scan rate of 0.1 mV s^{-1} . The galvanostatic charge–discharge tests were performed using a WMPG 3000 battery cyler system (WonATech Corp., Korea) in the potential range of 0.0–3.0 V (versus Li/Li^+) at $25 \text{ }^\circ\text{C}$ in an incubator. The cycle number dependence of the LIB cells was investigated for up to 50 cycles at a current density of 100 mA g^{-1} . The rate performance of the LIB cells was investigated at current densities of 100, 300, 500, 700, and 100 mA g^{-1} . The electrochemical impedance spectroscopy (EIS) measurements were measured by fresh cells in a frequency range of 100 kHz to 10 mHz at an AC signal of 5 mV.

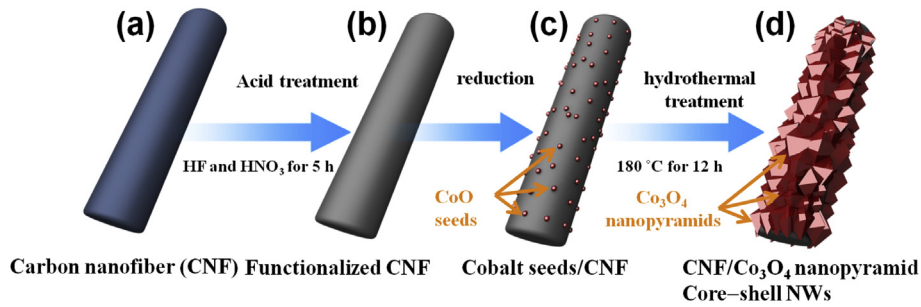


Fig. 1. Schematic illustration of the synthetic steps for (a) the CNFs using electrospinning, (b) functionalized CNFs using acid treatment, (c) CoO seeds/CNFs using reduction, and (d) CNF/Co₃O₄ nanopyramid core-shell NWs by a hydrothermal method.

3. Results and discussion

Fig. 1 shows the ideal schematic of the synthetic steps for CNF/Co₃O₄ nanopyramids core-shell NWs. As shown in **Fig. 1a**, the CNF was prepared using an electrospinning method with a PAN solution [30–35]. The resultant CNFs were then subjected to an acid treatment, which formed functional groups in order to strongly attach CoO seeds on the CNFs (**Fig. 1b**). CoO seeds/CNFs were then synthesized using a reduction method with cobalt nitrate (**Fig. 1c**). The CoO seeds attached on the CNFs were used as nucleation sites to form the Co₃O₄ nanopyramids during the hydrothermal reaction. Finally, CNF/Co₃O₄ nanopyramid core-shell NWs were synthesized using a hydrothermal method (**Fig. 1d**).

Fig. 2a–e show FESEM images of octahedral Co₃O₄, conventional CNFs, CoO seeds/CNFs, Co₃O₄/CNF composites, and CNF/Co₃O₄ nanopyramid core-shell NWs. The octahedral Co₃O₄, with diameters in the range of 0.8–1.2 μm, were formed using only the hydrothermal treatment method. The octahedral shape of Co₃O₄ particles is readily synthesized, as reported previously [29,40]. As shown in **Fig. 2b**, the conventional CNFs, with diameters in the range of 208–224 nm, exhibited smooth surfaces and uniform morphology. **Fig. 2c** shows the CoO seeds/CNFs used for the formation of Co₃O₄ nanopyramids on the CNFs. They are similar to the

conventional CNFs in that they have smooth surfaces and uniform morphology, implying that the CoO seeds were uniformly loaded onto the surfaces of the CNFs without aggregation of the CoO seeds. **Fig. 2d** shows FESEM images of the Co₃O₄/CNF composites, which are composed of octahedral Co₃O₄ and CNFs. It is noted that the CNFs penetrated into the octahedral Co₃O₄. Finally, **Fig. 2e** shows FESEM images of CNF/Co₃O₄ nanopyramid core-shell NWs synthesized by the hydrothermal treatment method with CoO seeds/CNFs; their diameter is in the range of 478–549 nm. The Co₃O₄ nanopyramids were uniformly grown on the CNF surfaces, with no empty surfaces or aggregation of Co₃O₄ nanopyramids. The insets of **Fig. 2d** and **e** show low-magnification FESEM images confirming the uniform formation of the Co₃O₄/CNF composites and CNF/Co₃O₄ nanopyramid core-shell NWs. Moreover, the diameter of the Co₃O₄ nanopyramids on the CNFs (193–245 nm) is lower than that of the octahedral Co₃O₄ and the Co₃O₄/CNF composites because CoO seeds on the CNFs provide many nucleation sites for the crystal growth of Co₃O₄. To clearly examine the morphological properties of the CNF/Co₃O₄ nanopyramid core-shell NWs, the cross-sectional FESEM images are shown in **Fig. 2f**. The interface between the CNFs (core region) and the Co₃O₄ nanopyramids (shell region) is closely connected with no empty space, which can contribute to improved electron transfer in the electrode for LIBs. The SEM results indicate

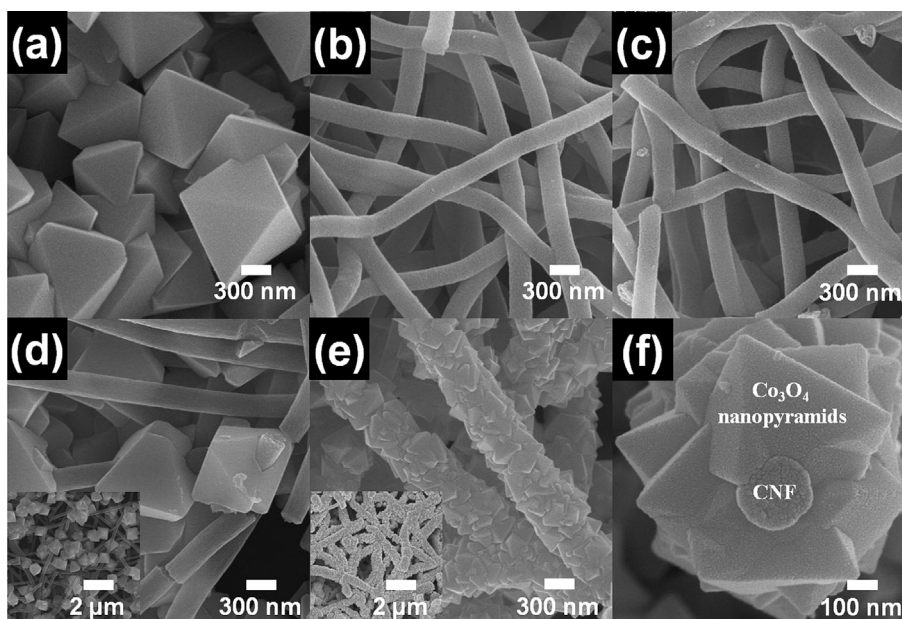


Fig. 2. SEM images of (a) octahedral Co₃O₄, (b) conventional CNFs, (c) CoO seeds/CNFs, (d) Co₃O₄/CNF composites, and (e) CNF/Co₃O₄ nanopyramid core-shell NWs. (f) A cross-sectional SEM image obtained from CNF/Co₃O₄ nanopyramid core-shell NWs (**Fig. 2e**).

that the Co_3O_4 nanopyramids were grown on CoO seeds on the CNFs, resulting in the successful formation of CNF/ Co_3O_4 nanopyramid core–shell NWs.

Fig. 3a–d show TEM images and high-resolution TEM images (shown in the insets) of conventional CNFs, CoO seeds/CNFs, Co_3O_4 /CNF composites, and CNF/ Co_3O_4 nanopyramid core–shell NWs. The conventional CNFs, shown in Fig. 3a, exhibit a uniform contrast because there is only one phase in the CNFs. However, the CoO seeds/CNFs exhibited relatively dark, nano-sized spots (~ 3 – 6 nm in size) on the CNF surfaces, implying the formation of CoO seeds on the CNFs via reduction (Fig. 3b). Fig. 3c shows TEM images of the Co_3O_4 /CNF composites, which have a hybrid structure consisting of octahedral Co_3O_4 (Fig. 3c, inset) and CNFs. However, the Co_3O_4 /CNF composites do not form to Co_3O_4 nanopyramids because of the absence of the cobalt seeds to act as nucleation sites on the CNFs. Fig. 3d shows TEM images of the CNF/ Co_3O_4 nanopyramid core–shell NWs, where Co_3O_4 nanopyramids are homogeneously formed on the CNFs with no empty spaces on the CNF surface. A high-resolution TEM image of the Co_3O_4 nanopyramids, shown in the inset of Fig. 3d, shows that the microstructure of the individual grains is clearly crystallized. Furthermore, the spacing of the lattice planes in the Co_3O_4 nanopyramids was observed to be ~ 0.242 nm, which corresponds to the (311) lattice plane of spinel Co_3O_4 (Fig. 3e). The inset of Fig. 3e shows the selected area electron diffraction (SAED) pattern of the CNF/ Co_3O_4 nanopyramid core–shell NWs, which displays clear rectangular reflection spots, indicating that Co_3O_4 is a cubic structure with adequate crystallinity.

Fig. 4a shows powder XRD data of the samples in order to investigate their crystallinities and crystalline phases. The reference bulk reflection of a pure Co_3O_4 phase is shown at the bottom of Fig. 4a. For the CNFs, only one broad diffraction peak, which corresponds to the (002) plane of the graphitic layer, is observed at approximately $2\theta = 25^\circ$ [41]. For CoO seeds/CNFs, a broad diffraction peak with no other diffraction peaks is observed because of the nano-sized scale and the small number of CoO seeds. The main characteristic diffraction peaks of the Co_3O_4 /CNF composites and CNF/ Co_3O_4 nanopyramid core–shell NWs are observed at 19.0° , 31.2° , 36.8° , 44.8° , 59.4° , and 65.2° , which corresponds to the (111),

(220), (311), (400), (511), and (440) planes, respectively. The XRD data are in good agreement with that of the Co_3O_4 phase with a cubic structure (space group $Fd\bar{3}m$ [227]; JCPDS card No. 78–1970). In particular, the oxygen source for forming the Co_3O_4 phase resulted from the hydrothermal reaction and heat treatment at 250°C in air. Furthermore, broad full width at half-maximum (FWHM) of the diffraction peaks for the CNF/ Co_3O_4 nanopyramid core–shell NWs is because of the reduced size of the Co_3O_4 nanopyramids as compared to the octahedral Co_3O_4 and the Co_3O_4 /CNF composites. The reduced size of the Co_3O_4 nanopyramids is owing to the increased number of nucleation sites provided by the formation of CoO seeds. These results are in good agreement with the SEM and TEM results. Furthermore, to investigate the chemical bonding states of the samples, Fig. 4b shows the XPS spectra analyzed using the Co $2p$ band shape. The Co $2p$ XPS spectral peaks of the octahedral Co_3O_4 , Co_3O_4 /CNFs, and CNF/ Co_3O_4 nanopyramid core–shell NWs exhibit two different signals at ~ 780.0 eV and ~ 795.0 eV, corresponding to the Co $2p_{3/2}$ and Co $2p_{1/2}$ photoelectrons, respectively, of the Co_3O_4 phase [42]. Also, the spin-energy separation of ~ 15 eV indicates a standard Co_3O_4 XPS spectra [43]. However, as compared to the above-mentioned three samples, the Co $2p_{3/2}$ and Co $2p_{1/2}$ photoelectrons for CoO seeds/CNFs are slightly shifted to higher binding energies of ~ 780.5 eV and ~ 795.7 eV, respectively, corresponding to the CoO phase [44]. The reason for the dominant form of the CoO phase is because of the restricted oxidation during the reduction process [45]. Owing to existence of CoO seeds relative to the nucleation sites, the Co_3O_4 nanopyramids could be uniformly and densely grown on the CoO seeds/CNFs using the hydrothermal method. This strategy has not been reported hitherto. Thus, the introduction of CoO seed-loaded CNFs can synthesize the different advanced structure compared to the previous works [21,22]. The contents and thermal stability of the samples were examined by TGA analysis, as shown in Fig. 4c. The conventional CNFs reached a weight loss of 100% up to 800°C , implying the presence of pure carbon materials without impurities. However, the CoO seeds/CNFs exhibited a weight loss of 93.9% owing to the existence of CoO seeds on the CNFs. Furthermore, the initial weight loss of CoO seeds/CNFs started at approximately

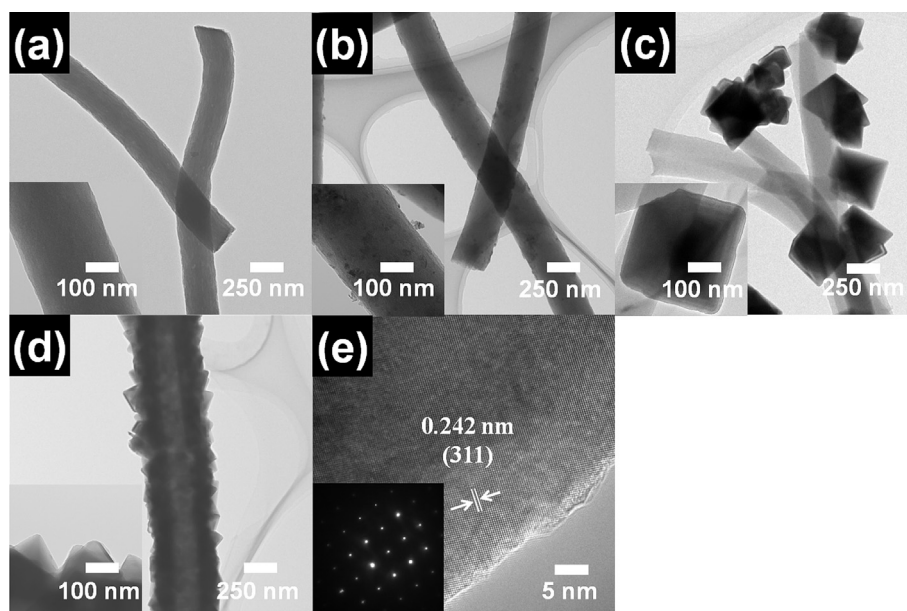


Fig. 3. TEM images of (a) conventional CNFs, (b) CoO seeds/CNFs, (c) Co_3O_4 /CNF composites, and (d) CNF/ Co_3O_4 nanopyramid core–shell NWs. High-resolution TEM images of the samples are shown in the inset of Fig. 3a–d, (e) A high-resolution TEM image and SAED pattern (inset) obtained from CNF/ Co_3O_4 nanopyramid core–shell NWs.

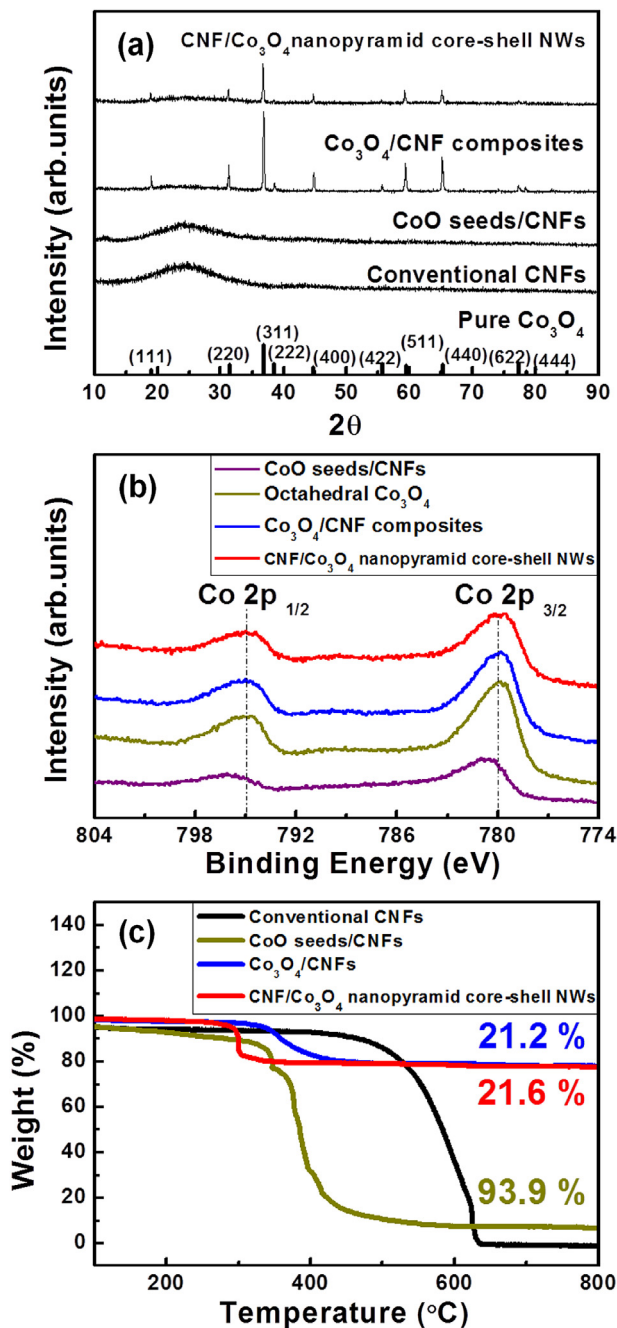


Fig. 4. (a) XRD patterns of the conventional CNFs, CoO seeds/CNFs, Co₃O₄/CNF composites, and CNF/Co₃O₄ nanopyramid core-shell NWs. (b) XPS spectra obtained from Co 2p band shape of the CoO seeds/CNFs, octahedral Co₃O₄, Co₃O₄/CNF composites, and CNF/Co₃O₄ nanopyramid core-shell NWs. (c) TGA curves of the conventional CNFs, CoO seeds/CNFs, Co₃O₄/CNF composites, CNF/Co₃O₄ nanopyramid core-shell NWs from 100 to 800 °C at a heating rate of 10 °C min⁻¹ in air atmosphere.

340 °C because of the relatively low thermal stability of the functional groups on the CNF surface as compared to the conventional CNFs. In addition, the Co₃O₄/CNF composites and CNF/Co₃O₄ nanopyramid core-shell NWs exhibited similar weight losses of 21.6% and 21.2%, which implies that although the two samples had the same weight ratio of CNFs and Co₃O₄, they had different morphologies.

To examine oxidation–reduction and reversibility of the electrodes, cyclic voltammetry (CV) measurements were performed

using a potentiostat/galvanostat in the potential range of 0.0–3.0 V (versus Li/Li⁺) at a scan rate of 0.1 mV s⁻¹, as shown in Fig. 5. For the CV curves of the conventional CNFs (Fig. 5a), a broad cathodic peak in the first discharge process of ~1.1 V, which is directly related to the formation of an irreversible solid electrolyte interface (SEI) layer on the CNF surface, is observed. The irreversible peak in the subsequent cycles tends to disappear. On the other hand, the CV curves of the octahedral Co₃O₄, Co₃O₄/CNF composites, and CNF/Co₃O₄ nanopyramid core-shell NWs in the first discharge process (Fig. 5b–d, respectively) exhibit cathodic peaks at ~0.85 V. These peaks can be explained by the SEI layer and the amorphous Li₂O phase formed during the reduction reaction of Co₃O₄ to metallic Co [46]. The observed anodic peaks in the first charge process at ~2.1 V for the octahedral Co₃O₄, Co₃O₄/CNF composites, and CNF/Co₃O₄ nanopyramid core-shell NWs are ascribed to the oxidation (delithiation) reaction of metallic Co to Co₃O₄ [47]. Thus, the overall electrochemical conversion reaction of Co₃O₄ in LIBs can be summarized as follows [49,50]:



In the case of the second and third discharge processes, the cathodic peaks of octahedral Co₃O₄, Co₃O₄/CNF composites, and CNF/Co₃O₄ nanopyramid core-shell NWs are shifted to the higher potential of 0.93 V, 0.94 V, and 1 V, respectively, because of the irreversible processes relative to the formation of an SEI layer and an amorphous Li₂O phase in the first discharge cycle [48]. In particular, for CV curves of the CNF/Co₃O₄ nanopyramid core-shell NWs (Fig. 5d), there are almost no differences in the CV curves between the second and third cycles as compared to the other samples, which indicates their excellent reversible capacity. That is, voltage interval of 1.1 V between the anodic and cathodic peaks in the second cycle of the CNF/Co₃O₄ nanopyramid core-shell NWs is the lowest value compared to those of octahedral Co₃O₄ (1.3 V) and Co₃O₄/CNF composites (1.2 V), which implies the reduced polarization of the electrodes. This phenomenon can be attributed to the improved electrical contact during Li-ion transfer because of the uniform and dense growth of Co₃O₄ nanopyramids on CNFs [26].

Fig. 6a–d show the galvanostatic charge–discharge curves of the cells fabricated with the conventional CNFs, octahedral Co₃O₄, Co₃O₄/CNF composites, and CNF/Co₃O₄ nanopyramid core-shell NWs, respectively, measured at a current density of 100 mA g⁻¹ in the voltage range of 0.0–3.0 V for the 1st, 2nd, 3rd, 10th, 30th, and 50th cycles. The conventional CNFs (Fig. 6a) show an inclined curve without the formation of a voltage plateau during the discharge process, indicating the typical discharge behavior of carbon-based materials [51]. However, the cells fabricated with octahedral Co₃O₄, Co₃O₄/CNF composites, and CNF/Co₃O₄ nanopyramid core-shell NWs (Fig. 6b–d, respectively) exhibit clear voltage plateaus at ~1.0 V in the first discharge curves. This phenomenon can be explained by the formation of amorphous Li₂O phases during the reduction reaction of Co₃O₄ to metallic Co. After reaching the plateau, the potential continuously drops to 0 V. In addition, the three samples (Fig. 6b–d, respectively) displayed two voltage plateaus of ~2.1 V in the first charge curves, corresponding to the reversible oxidation of metallic Co to Co₃O₄. During the first cycle, the specific charge and discharge capacities were respectively 313 and 571 mAh g⁻¹ for the conventional CNFs, 720 and 1034 mAh g⁻¹ for the octahedral Co₃O₄, 762 and 1040 mAh g⁻¹ for the Co₃O₄/CNF composites, and 995 and 1173 mAh g⁻¹ for the CNF/Co₃O₄ nanopyramid core-shell NWs. The initial large capacity loss during the first charge and discharge process occurred because of the formation of a SEI layer during the first discharge process. In particular, the conventional CNFs in our study (Fig. 6a) exhibited a capacity

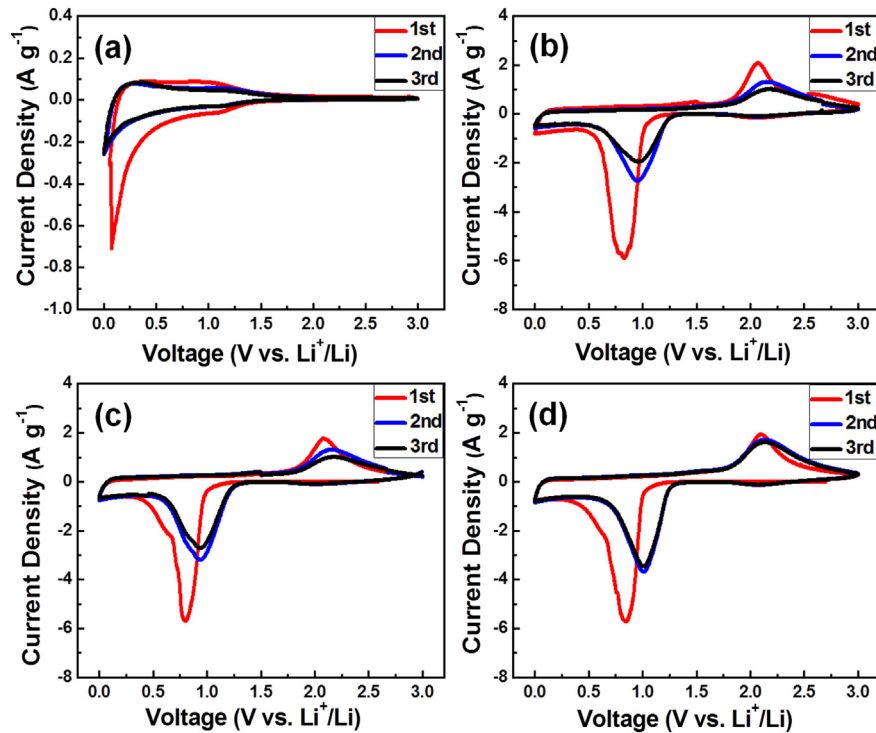


Fig. 5. CV curves of (a) the conventional CNFs, (b) octahedral Co_3O_4 , (c) $\text{Co}_3\text{O}_4/\text{CNF}$ composites, and (d) $\text{CNF}/\text{Co}_3\text{O}_4$ nanopyramid core–shell NWs measured using a potentiostat/galvanostat in the potential range of 0.0–3.0 V (versus Li^+/Li) at a scan rate of 0.1 mV s^{-1} .

similar to that found in previously reported studies [31,32]. For the octahedral Co_3O_4 electrodes, as the cycle number increased up to 50 cycles, their discharge capacity dramatically decreased, which is well known from previously reported studies [8,25,28,29].

Furthermore, the charge and discharge capacities of the $\text{Co}_3\text{O}_4/\text{CNF}$ composite electrode (Fig. 6c) were 263 and 264 mAh g^{-1} , respectively, after 50 cycles. This result indicates an improved capacity owing to the hybrid structures consisting of octahedral Co_3O_4 and

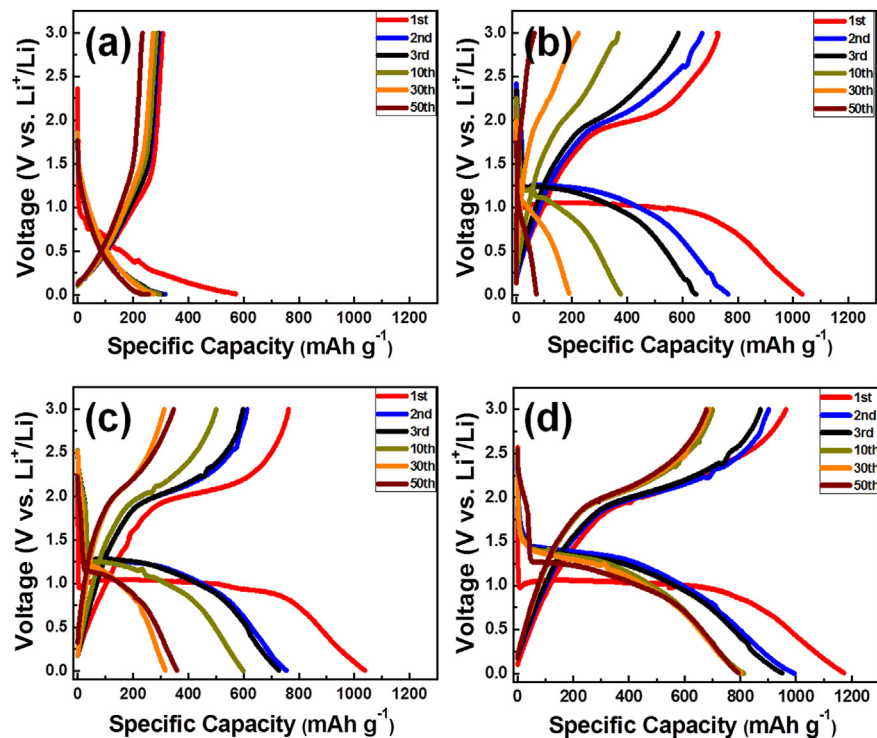


Fig. 6. Galvanostatic charge–discharge curves of the LIB cells fabricated with (a) the conventional CNFs, (b) octahedral Co_3O_4 , (c) $\text{Co}_3\text{O}_4/\text{CNF}$ composites, and (d) $\text{CNF}/\text{Co}_3\text{O}_4$ nanopyramid core–shell NWs, which measured at a current density of 100 mA g^{-1} in the potential range of 0.0–3.0 V for 1st, 2nd, 3rd, 10th, 30th and 50th cycles.

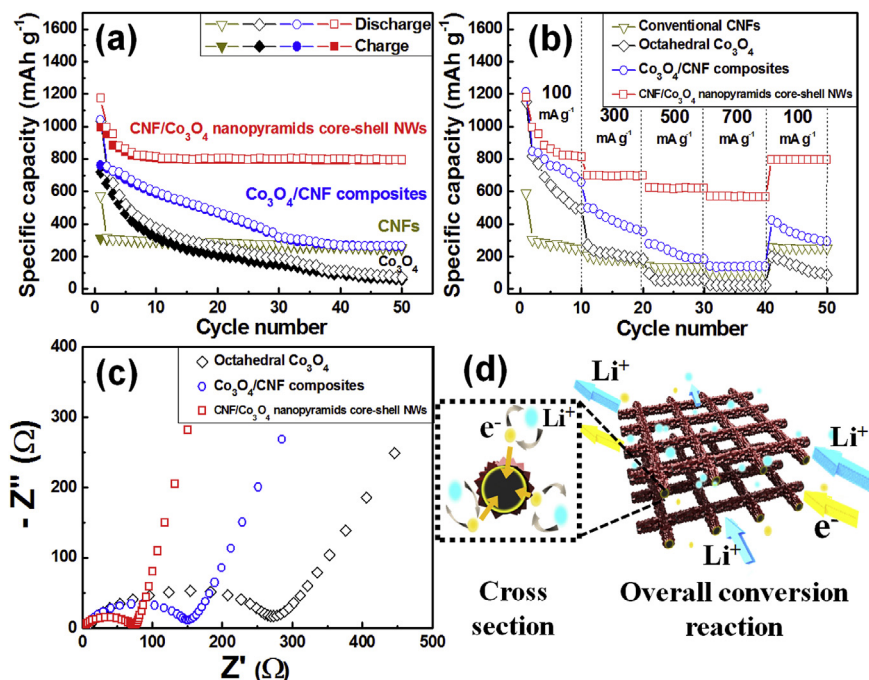


Fig. 7. (a) The cycling number dependence of the conventional CNFs, octahedral Co_3O_4 , CNFs, $\text{Co}_3\text{O}_4/\text{CNF}$ composites, and CNF/ Co_3O_4 nanopyramid core-shell NWs up to 50th cycles at a current density of 100 mA g^{-1} . (b) The rate performance of the conventional CNFs, octahedral Co_3O_4 , $\text{Co}_3\text{O}_4/\text{CNF}$ composites, and CNF/ Co_3O_4 nanopyramid core-shell NWs obtained from current densities of 100, 300, 500, 700, and 100 mA g^{-1} . (c) Nyquist plots of the Co_3O_4 , $\text{Co}_3\text{O}_4/\text{CNF}$ composites, and CNF/ Co_3O_4 nanopyramid core-shell NWs in the frequency range of 100 kHz to 10 mHz before the charge–discharge tests. (d) Ideal schematic illustration of the overall conversion reaction for the transfer of Li ions and electrons in CNF/ Co_3O_4 nanopyramid core-shell NWs.

CNFs as compared to the octahedral Co_3O_4 and the conventional CNF electrodes. In particular, the CNF/ Co_3O_4 nanopyramid core-shell NWs (Fig. 6d) exhibited superb charge and discharge capacities of 790 and 795 mAh g^{-1} , respectively, after 50 cycles, resulting in high-performance LIBs.

Fig. 7a shows the cycle number dependence of the charge–discharge capacities of LIB cells fabricated with all the samples. For the conventional CNF electrodes after one cycle, a low reversible capacity of 258 mAh g^{-1} remained almost constant up to 50 cycles. For the octahedral Co_3O_4 and $\text{Co}_3\text{O}_4/\text{CNF}$ composite electrodes, the reversible capacities decreased continuously up to 50 cycles. However, for the CNF/ Co_3O_4 nanopyramid core-shell NWs, their reversible capacities decreased slowly up to 5 cycles, and then remained almost constant at $\sim 795 \text{ mAh g}^{-1}$ up to 50 cycles. Furthermore, the initial Coulombic efficiency of the conventional CNFs, octahedral Co_3O_4 , $\text{Co}_3\text{O}_4/\text{CNF}$ composites, and CNF/ Co_3O_4 nanopyramid core-shell NWs was 54.8, 69.6, 73.2, and 84.8%, respectively. This implies that the CNF/ Co_3O_4 nanopyramid core-shell NWs displayed excellent reversible capacity as compared to the other samples. Table 1 summarizes the charge capacity, discharge capacity, the initial Coulombic efficiency, and reversible capacity of all the samples measured at a current density of 100 mA g^{-1} .

Fig. 7b shows the rate performance of all the samples obtained from current densities of 100, 300, 500, 700, and 100 mA g^{-1} . The octahedral Co_3O_4 and $\text{Co}_3\text{O}_4/\text{CNF}$ composites exhibited serious degradation of the reversible capacity with different current densities, indicating the poor high-rate capability of the electrodes. However, the CNF/ Co_3O_4 nanopyramid core-shell NWs maintained the best high-rate capability for reversible capacity. That is, their reversible capacities remained almost constant up to a high current density of 700 mA g^{-1} and then recovered to a high reversible capacity of 798 mAh g^{-1} when the current density decreased again to 100 mA g^{-1} . Therefore, the CNF/ Co_3O_4 nanopyramid core-shell NWs revealed a superb high-rate capability as compared to the other samples. As a result, the reversible capacity of the CNF/ Co_3O_4 nanopyramid core-shell NWs was in line with other reports on Co_3O_4 -based electrodes. However, after 50 cycles the core-shell NW electrode showed better cycle stability and excellent high-rate capability compared to the previously reported results due to the introduction of one-dimensional CNFs relative to efficient electron transport in the core region and high utilization of Co_3O_4 nanopyramids with high capacity grown closely and densely on the CNFs in the shell region [20,23,27–29,50].

Electrochemical impedance spectroscopy (EIS) measurements were carried out in order to determine the behavior for Li ion

Table 1
Summary of charge capacity, discharge capacity, the initial Coulombic efficiency, and reversible capacity for the conventional CNFs, octahedral Co_3O_4 , $\text{Co}_3\text{O}_4/\text{CNF}$ composites, and CNF/ Co_3O_4 nanopyramid core-shell NWs measured at a current density of 100 mA g^{-1} .

| Samples | Charge capacity at the first cycle (mAh g^{-1}) | Discharge capacity at the first cycle (mAh g^{-1}) | Initial coulombic efficiency (%) | Reversible capacity up to 50 cycles (mAh g^{-1}) |
|---|--|---|----------------------------------|---|
| Conventional CNFs | 313 | 571 | 54.8 | 256 |
| Octahedral Co_3O_4 | 720 | 1034 | 69.6 | 71 |
| $\text{Co}_3\text{O}_4/\text{CNF}$ composites | 762 | 1040 | 73.2 | 264 |
| CNF/ Co_3O_4 nanopyramid core-shell NWs | 995 | 1173 | 84.8 | 795 |

transfer. Fig. 7c shows the Nyquist plots of the electrodes in the frequency range of 100 kHz to 10 mHz before the charge–discharge tests. The semicircle in the medium-frequency range is attributed to the charge transfer impedance (R_{ct}) at the electrode/electrolyte interface, and the inclined line corresponds to the Li ion diffusion process in the electrodes, which is called the Warburg impedance. As shown in Fig. 7c, the CNF/ Co_3O_4 nanopyramid core–shell NWs displays a much smaller semicircle than the octahedral Co_3O_4 and Co_3O_4 /CNF composite electrodes, implying that the CNFs combined closely with the Co_3O_4 nanopyramids enhanced the electrical conductivity of the electrode [25,26,52]. Also, the CNF/ Co_3O_4 nanopyramid core–shell NWs and Co_3O_4 /CNF composite electrodes exhibit lower Warburg impedance than the octahedral Co_3O_4 ; this indicates excellent Li ion diffusion because of the network structure that provides increased contact area between the electrolyte and the electrode.

Fig. 7d shows the ideal schematic illustration of the electrodes fabricated with CNF/ Co_3O_4 nanopyramid core–shell NWs. As shown in the cross-sectional illustration, CNF/ Co_3O_4 nanopyramid core–shell NWs provide efficient electron transport because of the very close connection between the Co_3O_4 nanopyramids and the CNFs (Fig. 7d, left). In addition, the network structures (Fig. 7d, right) of the electrodes improved Li ion diffusion during the cycle process because of the increased contact area between the electrolyte and electrode [53,54].

Therefore, in this study, the superb electrochemical performance, including charge–discharge capacity, cycle stability, the initial Coulombic efficiency, and high-rate capability, for CNF/ Co_3O_4 nanopyramid core–shell NWs is successfully demonstrated. There are three reasons for the performance improvement: (I) introduction of 1-D CNFs relative to efficient electron transport in the core region, (II) high utilization of high capacity Co_3O_4 nanopyramids grown closely and densely on CNFs in the shell region, and (III) the network structures of the CNF/ Co_3O_4 core–shell electrodes relative to the improvement of the Li ion diffusion. These results indicate that electrodes fabricated with CNF/ Co_3O_4 nanopyramid core–shell NWs are excellent candidates as anode materials for high-performance LIBs.

4. Conclusions

CNF/ Co_3O_4 nanopyramid core–shell NWs were successfully synthesized using an electrospinning method followed by reduction and hydrothermal treatment. Co_3O_4 nanopyramids were grown closely and densely using CoO seeds on the CNFs. For comparison, conventional CNFs, octahedral Co_3O_4 , and Co_3O_4 /CNF composite electrodes were prepared. The electrode fabricated with CNF/ Co_3O_4 nanopyramid core–shell NWs exhibited superb discharge capacity (1173 mAh g^{-1}) after the first cycle and cycle stability (795 mAh g^{-1}) after 50 cycles, high initial Coulombic efficiency (84.8%), and excellent high-rate capability (570 mAh g^{-1} at 700 mA g^{-1}) as compared with conventional CNFs, octahedral Co_3O_4 , and Co_3O_4 /CNF composite electrodes. The superb electrochemical performance is because of the synergistic effect of 1-D CNFs relative to efficient electron transport in the core region, high utilization of high capacity Co_3O_4 nanopyramids in the shell region, and the geometric network structures of the electrodes relative to the improvement of the Li ion diffusion.

Acknowledgments

This research was supported by Basic Science Research Program through the National Research Foundation of Korea (NRF) funded by the Ministry of Education, Science and Technology (2012–007444).

References

- [1] S. Goriparti, E. Miele, F.D. Angelis, E.D. Fabrizio, R.P. Zaccaria, C. Capiglia, *J. Power Sources* 257 (2014) 421–443.
- [2] M. Armand, J.M. Tarascon, *Nature* 451 (2008) 652–657.
- [3] C. Casas, W. Li, *J. Power Sources* 208 (2012) 74–85.
- [4] G. Zhang, H.B. Wu, H.E. Hoster, X.W. Lou, *Energy Environ. Sci.* 7 (2014) 302–305.
- [5] A. Barré, B. Deguilhem, S. Grolleau, M. Gérard, F. Suard, D. Riu, *J. Power Sources* 241 (2013) 680–689.
- [6] W. Wei, Z. Wang, Z. Liu, Y. Liu, L. He, D. Chen, A. Umar, L. Guo, J. Li, *J. Power Sources* 238 (2013) 376–387.
- [7] F. Cheng, J. Liang, Z. Tao, J. Chen, *Adv. Mater.* 23 (2011) 1695–1715.
- [8] L. Li, G. Zhou, X.-Y. Shan, S. Pei, F. Li, H.-M. Cheng, *J. Power Sources* 255 (2014) 52–58.
- [9] M. Shahid, N. Yesibolati, M.C. Reuter, F.M. Ross, H.N. Alshareef, *J. Power Sources* 263 (2014) 239–245.
- [10] Z. Bi, M.P. Paranthaman, P.A. Menchhofer, R.R. Dehoff, C.A. Bridges, M. Chi, B. Guo, X.-G. Sun, S. Dai, *J. Power Sources* 222 (2013) 461–466.
- [11] C. Wu, X. Li, W. Li, B. Li, Y. Wang, Y. Wang, M. Xu, L. Xing, *J. Power Sources* 251 (2014) 85–91.
- [12] Q. Zhang, J. Wang, D. Xu, Z. Wang, X. Li, K. Zhang, *J. Mater. Chem. A* 2 (2014) 3865–3874.
- [13] Y.S. Yun, J.M. Kim, H.H. Park, J. Lee, Y.S. Huh, H.-J. Jin, *J. Power Sources* 244 (2013) 747–751.
- [14] P. Poizot, S. Laruelle, S. Grugeon, L. Dupont, J.M. Tarascon, *Nature* 407 (2000) 496–499.
- [15] Y. Lu, Y. Wang, Y. Zou, Z. Jiao, B. Zhao, Y. He, M. Wu, *Electrochem. Commun.* 12 (2010) 101–105.
- [16] X.Y. Xue, S. Yuan, L.L. Xing, Z.H. Chen, B. He, Y.J. Chen, *Chem. Commun.* 47 (2011) 4718–4720.
- [17] H. Sun, M. Ahmad, J. Zhu, *Electrochim. Acta* 89 (2013) 199–205.
- [18] J. Wang, B. Niu, G. Du, R. Zeng, Z. Chen, Z. Guo, S. Dou, *Mater. Chem. Phys.* 126 (2011) 747–754.
- [19] X. Xia, J.P. Tu, J.Y. Xiang, X.H. Huang, X.L. Wang, X.B. Zhao, *J. Power Sources* 195 (2010) 2014–2022.
- [20] J. Zheng, J. Liu, D. Lv, Q. Kuang, Z. Jiang, Z. Xie, R. Huang, L. Zheng, *J. Solid State Chem.* 183 (2010) 600–605.
- [21] W. Yao, J. Yang, J. Wang, L. Tao, *Electrochim. Acta* 53 (2008) 7326–7330.
- [22] W.-L. Yao, J.-L. Wang, J. Yang, G.-D. Dum, *J. Power Sources* 176 (2008) 369–372.
- [23] L. Fei, Q. Lin, B. Yuan, M. Naemi, Y. Xu, Y. Li, S. Deng, H. Luo, *Mater. Lett.* 98 (2013) 59–62.
- [24] L. Wang, Y. Yu, P.-C. Chen, C.-H. Chen, *Scr. Mater.* 58 (2008) 405–408.
- [25] B.G. Choi, S.J. Chang, Y.B. Lee, J.S. Bae, H.J. Kim, Y.S. Huh, *Nanoscale* 4 (2012) 5924–5930.
- [26] S.M. Abbas, S.T. Hussain, S. Ali, N. Ahmad, N. Ali, K.S. Munawar, *Electrochim. Acta* 105 (2013) 481–488.
- [27] J. Park, W.G. Moon, G.P. Kim, I. Nam, S. Park, Y. Kim, J. Yi, *Electrochim. Acta* 105 (2013) 110–114.
- [28] Y. Wang, F. Yan, S.W. Liu, A.Y.S. Tan, H. Song, X.W. Sun, H.Y. Yang, *J. Mater. Chem. A* 1 (2013) 5212–5216.
- [29] G. Zhou, L. Li, Q. Zhang, N. Li, F. Li, *Phys. Chem. Chem. Phys.* 15 (2013) 5582–5587.
- [30] Y. Li, B. Guo, L. Ji, Z. Lin, G. Xu, Y. Liang, S. Zhang, O. Toprakci, Y. Hu, M. Alcoutlabi, X. Zhang, *Carbon* 51 (2013) 185–194.
- [31] L. Zou, L. Gan, R. Lv, M. Wang, Z. Huang, F. Kang, W. Shen, *Carbon* 49 (2011) 89–95.
- [32] G.H. An, S.J. Kim, K.W. Park, H.J. Ahn, *Electrochem. Solid-State Lett.* 3 (2014) M21–M23.
- [33] G.H. An, H.J. Ahn, *Carbon* 65 (2013) 87–96.
- [34] G.H. An, H.J. Ahn, *Ceram. Int.* 38 (2012) 3197–3201.
- [35] J. Kong, Z. Liu, Z. Yang, H.R. Tan, S. Xiong, S.Y. Wong, X. Li, X. Lu, *Nanoscale* 4 (2012) 525–530.
- [36] B. Simon, S. Flandrois, K. Guerin, A. Fevrier-Bouvier, I. Teulat, P. Biensan, *J. Power Sources* 81–82 (1999) 312–316.
- [37] G.H. An, H.J. Ahn, *Electrochem. Solid-State Lett.* 2 (2013) M33–M36.
- [38] G.H. An, H.J. Ahn, *J. Electroanal. Chem.* 707 (2013) 74–77.
- [39] N. Kakati, J. Maiti, S.H. Jee, S.H. Lee, Y.S. Yoon, *J. Alloys Compd.* 509 (2011) 5617–5622.
- [40] G.L. Xu, J.T. Li, L. Huang, W. Lin, S.G. Sun, *Nano Energy* 2 (2013) 394–402.
- [41] C. Kim, K.S. Yang, M. Kojima, K. Yoshida, Y.J. Kim, Y.A. Kim, M. Endo, *Adv. Funct. Mater.* 16 (2006) 2393–2397.
- [42] L. Li, Y. Li, S. Gao, N. Koshizaki, *J. Mater. Chem.* 19 (2009) 8366–8371.
- [43] Z. Wen, L. Zhu, W. Mei, Y. Li, L. Hu, L. Sun, W. Wan, Z. Ye, *J. Mater. Chem. A* 1 (2013) 7511–7518.
- [44] G. Yang, D. Gao, Z. Shi, Z. Zhang, J. Zhang, J. Zhang, D. Xue, *J. Phys. Chem. C* 114 (2010) 21989–21993.
- [45] W.H. Ryu, J. Shin, J.W. Jung, I.D. Kim, *J. Mater. Chem. A* 1 (2013) 13203–13208.
- [46] A.K. Rai, J. Gim, L.T. Anh, J. Kim, *Electrochim. Acta* 100 (2013) 63–71.
- [47] D. Fang, L. Li, W. Xu, G. Li, G. Li, N. Wang, Z. Luo, J. Xu, L. Liu, C. Huang, C. Liang, Y. Ji, *J. Mater. Chem. A* 22 (2012) 15056–15061.
- [48] X.L. Yang, K.C. Fan, Y.H. Zhu, J.H. Shen, X. Jiang, P. Zhao, S.R. Luan, C.Z. Li, *ACS Appl. Mater. Interfaces* 5 (2013) 997–1002.

- [49] S. Megahed, B. Scrosati, *J. Power Sources* 51 (1994) 79–104.
- [50] X.W. Lou, D. Deng, J.Y. Lee, J. Feng, L.A. Archer, *Adv. Mater.* 20 (2008) 258–262.
- [51] X. Zhao, D. Xia, J. Yue, S. Liu, *Electrochim. Acta* 116 (2014) 292–299.
- [52] J. Chen, X. Xia, J. Tu, Q. Xiong, Y.X. Yu, X. Wang, C. Gu, *J. Mater. Chem.* 22 (2012) 15056–15061.
- [53] B. Zhao, S. Jiang, C. Su, R. Cai, R. Ran, M.O. Tadé, Z. Shao, *J. Mater. Chem. A* 1 (2013) 12310–12320.
- [54] M. Zhang, E. Uchaker, S. Hu, Q. Zhang, T. Wang, G. Cao, J. Li, *Nanoscale* 5 (2013) 12342–12349.